Effect of Flow on the Corrosion Behavior of Pipeline Steel in Supercritical CO_2 Environments with Impurities

Yoon-Seok Choi,‡, Martin Colahan,* and Srdjan Nešić**

Corrosion is a major concern in transmission pipelines that transport captured CO_2. While dry CO_2 is noncorrosive, significant corrosion has been reported in dense-phase CO_2 with trace amounts of water and impurities such as O_2, H_2S, SO_x, and NO_x. The aim of this work is to improve our understanding of the physicochemical aspects of the corrosion of carbon steels in the high-pressure environments associated with CO_2 transmission pipelines. The effect of flow on the corrosion of X65 carbon steel was investigated in a series of autoclave tests with different combinations of impurity concentrations in supercritical CO_2 conditions (8 MPa and 35°C). The corrosion rate of specimens was determined by weight loss measurements. The surface morphology and composition of the corrosion product layers were characterized using surface analytical techniques (scanning electron microscopy, eneregy dispersive x-ray spectroscopy, and Raman microscopy). Localized corrosion was measured via surface profilometry after corrosion products were removed. Results showed that no corrosion was observed in the supercritical CO_2 with 650 ppm_v of water, 50 ppm_v SO_2, and 100 ppm_v NO, but corrosion occurred when SO_2 concentration was increased to 4,500 ppm_v and 40,000 ppm_v of O_2 was added to the system. The presence of flow significantly accelerated the corrosion of carbon steel. Furthermore, localized corrosion was observed in the presence of both O_2 and flow.

KEY WORDS: carbon capture and storage, carbon steel, corrosion, impurities, supercritical carbon dioxide

INTRODUCTION

The availability of infrastructure that can securely and efficiently transport CO_2 is critical for carbon capture and storage (CCS) deployment. Pipelines are the most cost-effective way to transport vast amounts of CO_2 onshore and offshore, depending on distance and volume. Pipeline transportation has been practiced for many years and is now widely used. However, transporting CO_2 streams with impurities, rather than pure CO_2 streams, presents additional challenges. Several studies have shown that when transporting captured CO_2 containing impurities, different factors such as operating pressure, depressurization times, and pipe integrity should be considered.[1-2]

Corrosion plays an important role in the integrity management of the CO_2 transport pipeline as carbon steels, the most common material utilized for pipeline construction, are susceptible to corrosion in the presence of impurities. It is well known that dry CO_2 does not corrode carbon steels, and negligible corrosion occurred at water-unsaturated conditions (below solubility level) in dense-phase CO_2 (liquid and supercritical).[3-7] However, it has been reported that noticeable, and potentially severe, corrosion occurs at water-unsaturated conditions in dense-phase CO_2 with the presence of impurities, such as O_2, H_2S, SO_2, NO_2, etc., due to synergisms between chemical species. Hua, et al.,[8-9] reported that general corrosion rates ranged from 0 mm/y to 0.012 mm/y with water contents varying from 300 ppm_v to 2,800 ppm_v in the supercritical CO_2 with 1,000 ppm_v O_2. They also found that the general corrosion rates of X65 steel increased from 0.01 mm/y to 0.06 mm/y with water concentration increasing from 300 ppm_v to 1,770 ppm_v with 100 ppm_v SO_2 and 20 ppm_v O_2 at 35°C and 8 MPa. Xu, et al.,[10] reported that the general corrosion rates of carbon steels (X60, X65, X70, and X80) varied from 0.01 mm/y to 0.94 mm/y at water contents ranging from 1,600 ppm_v to 3,000 ppm_v at 10 MPa CO_2 and 50°C with 3,000 ppm_v SO_2 and 1,000 ppm_v O_2. Dugstad, et al.,[11] investigated the corrosion behavior of carbon steel exposed to liquid CO_2 flow at 10 MPa and 25°C. The results showed that there was no corrosion in the liquid CO_2 flow with 1,222 ppm_v H_2O while adding 344 ppm_v SO_2-induced corrosion at a rate of 0.02 mm/y and adding 478 ppm_v NO_2 caused severe corrosion with rates reaching 1.6 mm/y. Farelas, et al.,[12] observed no corrosion when the water is kept below its solubility limit in supercritical and liquid CO_2. However, a corrosion rate of 3.5 mm/y was measured in the presence of 1% SO_2 with 650 ppm_v H_2O at 8 MPa and 50°C. Furthermore, localized attacks were seen with a rate of 6.8 mm/y in the presence of 0.1% SO_2. Choi, et al.,[13] investigated the effect of H_2S on the corrosion behavior of pipeline steels in high-pressure CO_2 systems. The results showed that the general corrosion rates of the carbon steel and 1Cr steel tested were below 0.01 mm/y with the presence of 100 ppm_v H_2O and 200 ppm_v H_2S in the liquid (12 MPa, 25°C) and supercritical (12 MPa, 80°C) CO_2 phases. Sun, et al.,[14] determined the water content limit and the effect of water content on the corrosion mechanisms of X65 steel in supercritical CO_2-H_2O-O_2-H_2S-SO_2 environments. The corrosion rate of carbon steel increased from 0.0036 mm/y with 200 ppm_v of H_2O to 0.55 mm/y with 4,333 ppm_v of H_2O containing 200 ppm_v O_2, 200 ppm_v SO_2,

Submitted for publication: September 8, 2022. Revised and accepted: March 12, 2023. Preprint available online: March 12, 2023, https://doi.org/10.5006/4199.
‡ Corresponding author. E-mail: choiy@ohio.edu.
* Institute for Corrosion and Multiphase Technology, Department of Chemical & Biomolecular Engineering, Ohio University, Athens, Ohio 45701.

ISSN 0010-9312 (print), 1938-159X (online)

Table 1. *Element Analysis for the UNS K03014 Carbon Steel Used in the Tests (wt%)*

C	Mn	Si	P	S	Cr	Cu	Ni	Mo	Al
0.065	1.54	0.25	0.013	0.001	0.05	0.04	0.04	0.007	0.041

and 200 ppm_v H_2S at 10 MPa CO_2 and 50°C. Morland, et al.,[15-17] studied corrosion and chemical reactions in dense-phase CO_2 with multiple impurities (H_2O, SO_2, O_2, H_2S, and NO_2). A low corrosion rate of 0.07 mm/y was measured at 9.8 MPa CO_2 and 25°C with 90 ppm_v H_2O, 70 ppm_v O_2, 30 ppm_v SO_2, 36 ppm_v H_2S, and 32 ppm_v NO_2. With 670 ppm_v H_2O and 75 ppm_v NO_2, the corrosion rate was found to be 0.55 mm/y at 10 MPa CO_2 and 25°C, and the corrosion rate decreased to 0.003 mm/y with 1,900 ppm_v H_2O, 75 ppm_v SO_2, and 230 ppm_v O_2. Recently, they also suggested that a separate corrosive liquid phase containing H_2SO_4 and HNO_3 formed when the impurity concentration exceeded 35 ppm_v of SO_2, NO_2, H_2S, and O_2 at water-unsaturated conditions (10 MPa CO_2 and 25°C).

Considering that the application of the aforementioned studies is the internal corrosion of pipelines related to CCS, enhanced oil recovery (EOR), and deep-water oil and gas production, an attempt to evaluate the effect of flow on the corrosion behavior must also be made. Liu, et al.,[18] investigated the effect of flow rate on steel corrosion in supercritical CO_2 with different water concentrations. The results showed that a higher flow rate significantly enhanced the corrosion rate of carbon steel related to a mechanism of water droplet entrainment. de Sa, et al.,[19] investigated the effect of flow rate on the corrosion behavior of carbon steel in water-saturated supercritical CO_2 environments (8 MPa and 35°C). The uniform general corrosion rate was not enhanced in the presence of fluid flow; however, the measured pitting penetration rates were up to one order of magnitude higher than the uniform corrosion rates. A rotating cage-like device was used to create dynamic conditions. However, they investigated only the effect of water without considering other impurities.

There are very limited data on steel corrosion behavior in flowing supercritical CO_2 conditions with different impurities. Thus, the objective of the present study was to identify and quantify the effect of flow on the integrity of carbon steel in supercritical CO_2 with different impurities, specifically H_2O, SO_2, O_2, and NO.

EXPERIMENTAL PROCEDURES

2.1 | Material and Electrolyte

The test specimens were machined from (UNS K03014[(1)]) low carbon steel with a size of 12 mm × 12 mm × 2.5 mm for the quiescent tests and 25.4 mm × 12.5 mm × 3.1 mm for the flowing tests. A small hole at one end served to hang the samples from a sample stand with nonmetallic spacers. The composition of the steel used in the present study was given in Table 1. The specimens were polished with 600 grit silicon carbide paper, cleaned with alcohol in an ultrasonic bath, dried, and weighed using a balance with a precision of 0.1 mg. The electrolyte used in this work was deionized (DI) water.

2.2 | Autoclave Setup with Impurity Injection System

Experiments were performed in a high-pressure system, consisting of a 7.5 L Hastelloy autoclave, an impurity injection system, and a high-pressure CO_2 booster pump. Schematic drawings of the high-pressure system were shown in Figure 1. After the lid was attached, the autoclave was purged by multiple cycles of pressurization with CO_2 and then depressurization. The required volume of N_2-sparged DI water was then added using a micropipette just prior to pressurization with impurities and CO_2. The impurities were added from technical grade (ultrahigh purity) sulfur dioxide (SO_2), nitric oxide (NO), and oxygen (O_2) cylinders with a custom-built gas injection system (Figure 1[a]). For trace quantities of impurity gas, the moles of gas required were obtained by injecting the gas into a cylinder of known volume at a known temperature and pressure. The gas was then pushed into the autoclave with CO_2. Gases at higher concentrations were injected directly into the autoclave until the required ΔP was obtained. The moles of each impurity (n_i) that was necessary to achieve the required concentrations were calculated from the total mole of the mixture (n) from the real gas law:

$$n = \frac{PV}{ZRT} \quad (1)$$

$$n_i = y_i n \quad (2)$$

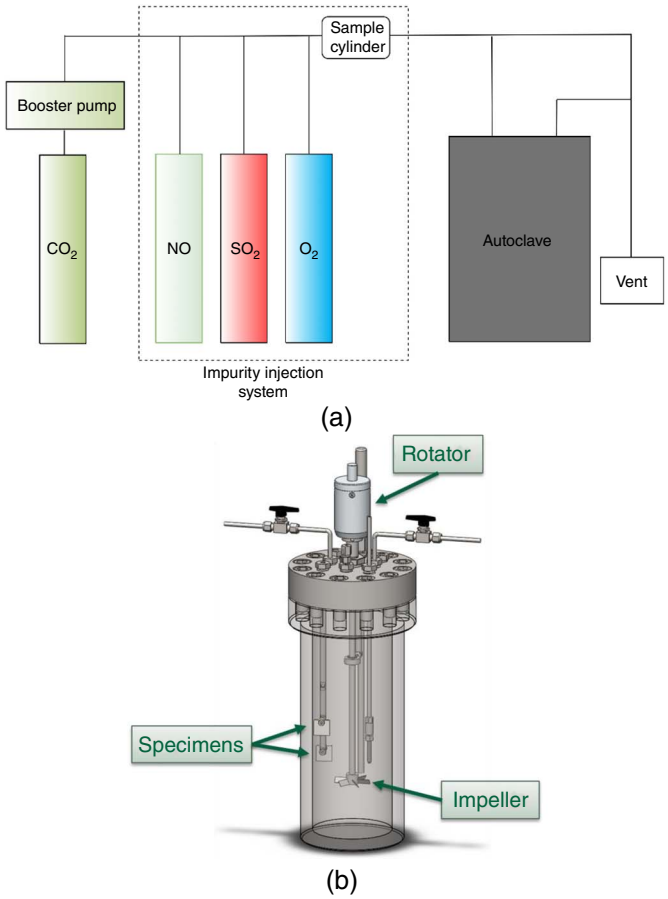

FIGURE 1. *Schematic drawings of the autoclave system used for corrosion testing: (a) high-pressure system and (b) autoclave.*

(1) UNS numbers are listed in *Metals & Alloys in the Unified Numbering System*, published by the Society of Automotive Engineers (SAE International) and cosponsored by ASTM International.

where P is the total pressure, V is the volume of the autoclave, Z is the compressibility factor of the mixture, R is the gas constant, T is the testing temperature, and y_i is the mole fraction of each impurity. Z was calculated by using Peng-Robinson equation of state.[20] High-pressure CO_2 sourced from high-purity bottles was added to the autoclave, aided with a gas booster pump, to the desired working pressure. An impeller was used to stir the supercritical CO_2 and to generate flow velocities of about 1 m/s (1,000 rpm) during the test for the conditions with flow (Figure 1[b]).

2.3 | Methodology

The corrosion rates were determined by weight-loss methods at the end of 48 h of exposure. The specimens were removed and cleaned for 5 min in Clarke's solution (20 g antimony trioxide + 50 g stannous chloride and hydrochloric acid to make 1,000 mL) to remove corrosion products. The specimens were then rinsed in distilled water, dried, and weighed to 0.1 mg. The corrosion rate is then calculated by the following equation:[21]

$$\text{Corrosion rate (mm/y)} = \frac{8.76 \times 10^4 \text{ (mm} \cdot \text{h/cm} \cdot \text{y)} \times \text{weight loss (g)}}{\text{surface area (cm}^2\text{)} \times \text{density (g/cm}^3\text{)} \times \text{time (h)}} \quad (3)$$

Following extraction, the morphology and compositions of corrosion products were analyzed by scanning electron microscopy (SEM), energy dispersive x-ray spectroscopy (EDS), and Raman spectroscopy. Localized corrosion was characterized via surface profilometry after corrosion products were removed. Table 2 showed the detailed test conditions for the present study. The concentrations of impurities were set upon autoclave closure and left to proceed naturally without further additions; 650 ppm_v of H_2O concentration was fixed for all tests based on CO_2 specifications[22-23] which created a water-unsaturated condition at the testing pressure and temperature. The concentrations of SO_2, O_2, and NO were determined by considering worst-case scenarios in field conditions. At the end of each test, SO_2 and NO_2 concentrations were measured using Gastec colorimetric tubes.

RESULTS

3.1 | Effect of SO_2 and O_2 (Test 1 to Test 4)

Figure 2 shows the corrosion rates of carbon steel in the supercritical CO_2 phase with different concentrations of SO_2 and O_2 under quiescent conditions. There was no measurable sample weight change (less than 0.1 mg/cm^2) and no visible signs of corrosion after the test in the presence of 50 ppm_v of SO_2 with 650 ppm_v H_2O and 100 ppm_v NO (test 1), indicating an insignificant corrosion rate. However, a moderate corrosion rate was measured (~0.15 mm/y) when the SO_2 concentration increased to 4,500 ppm_v (test 2). This corrosion rate is slightly higher than the previous experiments (≈0.1 mm/y) conducted at a lower SO_2 concentration (1,000 ppm_v).[12] It is noteworthy that the corrosion rates increased with the addition of 40,000 ppm_v O_2 for both low (50 ppmv) and high (4,500 ppmv) SO_2 concentrations (test 3 and test 4). This has previously been postulated to be due to the formation of sulfuric acid (H_2SO_4) in the presence of O_2.[24]

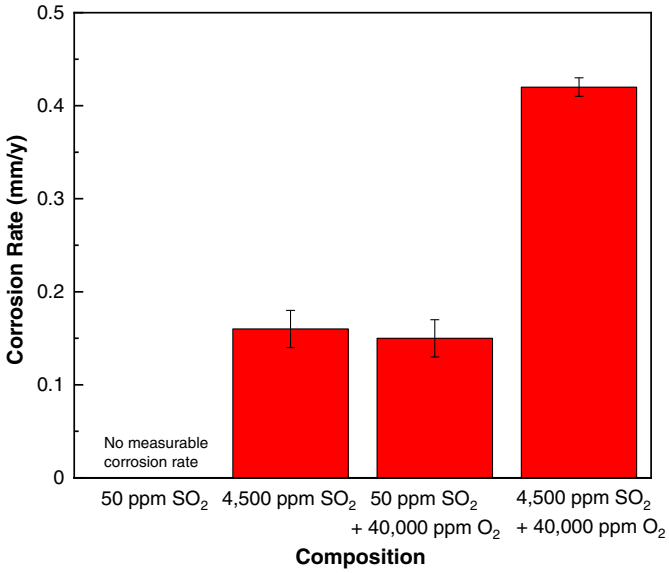

FIGURE 2. *Corrosion rates of X65 carbon steel under supercritical CO_2 with different SO_2 and O_2 concentrations in quiescent conditions.*

Figure 3 shows the SEM image and EDS spectra of the surface of the specimen from test 2 after 48 h of exposure in the supercritical CO_2 phase with 650 ppm_v H_2O, 4,500 ppm_v SO_2, and 100 ppm_v NO. The surface was covered by scattered corrosion products with cracks, which clearly show the occurrence of corrosion under the testing condition. EDS analyses of corrosion product (location A in Figure 3[a]) showed that it mainly consisted of iron (Fe), oxygen (O), and sulfur (S) (Figure 3[b]), suggesting the formation of $FeSO_3$ as seen in other studies.[9,12,24] Furthermore, areas where no corrosion

Table 2. *Test Conditions for Corrosion Testing (Concentrations are Initial Values Set upon Autoclave Closure)*

Test	Material	pCO_2 (MPa)	Temperature (°C)	H_2O (ppm_v)	SO_2 (ppm_v)	NO (ppm_v)	O_2 (ppm_v)	Flow
1	X65	8	35	650	50	100	0	No
2	X65	8	35	650	4,500	100	0	No
3	X65	8	35	650	50	100	40,000	No
4	X65	8	35	650	4,500	100	40,000	No
5	X65	8	35	650	4,500	100	0	Yes
6	X65	8	35	650	4,500	100	20,000	Yes
7	X65	8	35	650	4,500	100	40,000	Yes
8	X65	8	35	650	50	100	40,000	Yes

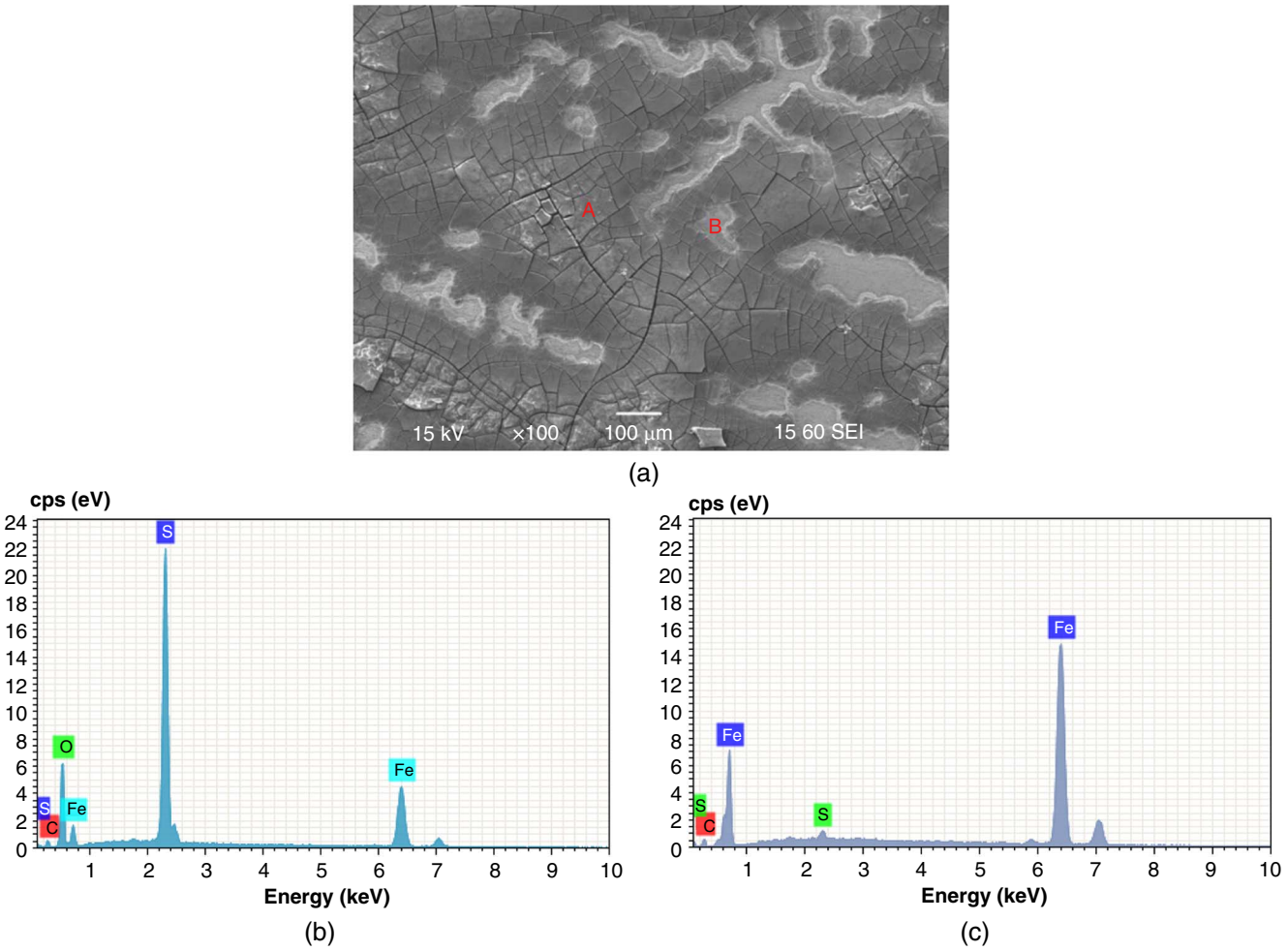

FIGURE 3. *SEM image and EDS spectra of the corroded surface of a sample exposed to the supercritical CO_2 phase with 650 ppm_v H_2O, 4,500 ppm_v SO_2, and 100 ppm_v NO for 48 h (test 2): (a) SEM surface image, (b) EDS spectrum of location A, and (c) EDS spectrum of location B.*

products were formed were also observed (location B in Figure 3[a]), where the main element is Fe as shown in the result of EDS analysis (Figure 3[c]).

Figure 4 shows the SEM image and EDS spectra of the surface of the sample from test 3 after 48 h of exposure in the supercritical CO_2 phase with 650 ppm_v H_2O, 50 ppm_v SO_2,

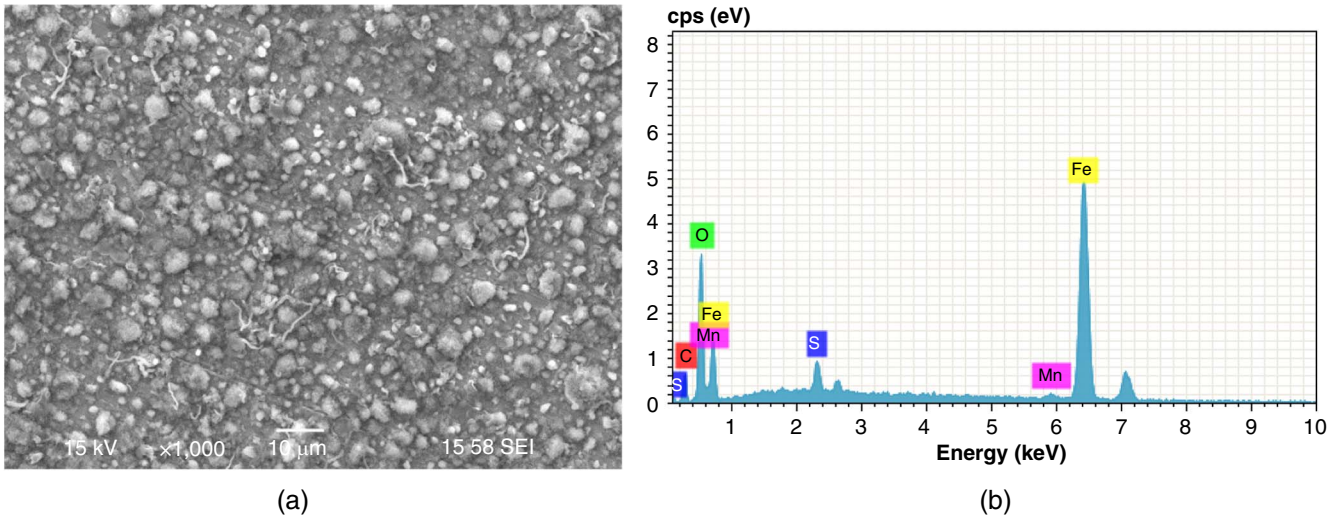

FIGURE 4. *(a) SEM image and (b) EDS spectrum of the corroded surface of a sample exposed to the supercritical CO_2 phase with 650 ppm_v H_2O, 50 ppm_v SO_2, 100 ppm_v NO, and 40,000 ppm_v O_2 for 48 h (test 3).*

100 ppm_v NO, and 40,000 ppm_v O_2. The surface was uniformly covered by thin corrosion products, which mainly consisted of phases that were comprised of Fe, O, and S. It is noteworthy that the concentration of S from EDS analysis of the corrosion products is quite low compared with Fe and O (Table 3), indicating that oxides can be present as well as $FeSO_4$; a typical corrosion product formed in the presence of SO_2 and O_2.

Figure 5 shows the SEM image and EDS spectra of the surface of the sample from test 4 after 48 h of exposure to the supercritical CO_2 phase with 650 ppm_v H_2O, 4,500 ppm_v SO_2, 100 ppm_v NO, and 40,000 ppm_v O_2. The surface was covered by thick corrosion products. EDS analysis of corrosion products showed that although the morphology of the corrosion product is different, the constituent elements are the same (Fe, O, and S). It also showed a low content of S, similar to the results of test 3 with 50 ppm_v SO_2 and 40,000 ppm_v O_2, indicating the formation of oxides (Table 4).

Table 3. *EDS Quantitative Analysis of the Corroded Surface Shown in Figure 4 (Test 3)*

Fe (at%)	C (at%)	S (at%)	O (at%)
51.06	17.53	2.20	27.59

Table 4. *EDS Quantitative Analysis for Different Locations of the Corroded Surface Shown in Figure 5 (Test 4)*

At%	Fe	C	S	O
A	46.11	9.19	1.30	43.40
B	38.70	15.61	3.77	41.93

Figure 6 shows the surface morphologies of samples after removing the corrosion products. No localized corrosion was observed on the surface (uniform corrosion) for all three tests (test 2 to test 4) with different concentrations of SO_2 and O_2 under quiescent conditions.

3.2 | Effect of Flow (Test 5 to Test 8)

Figure 7 shows the corrosion rates of carbon steel in the flowing supercritical CO_2 phase (650 ppm_v H_2O, 4,500 ppm_v SO_2, and 100 ppm_v NO) with different O_2 concentrations (test 5 to test 7). Compared with the corrosion rate without flow, the presence of flow increased the corrosion rates. Although the addition of 20,000 ppm_v O_2 does not affect the general corrosion rate under flowing conditions, the corrosion rate significantly increased to approximately 7 mm/y when 40,000 ppm_v O_2 was added.

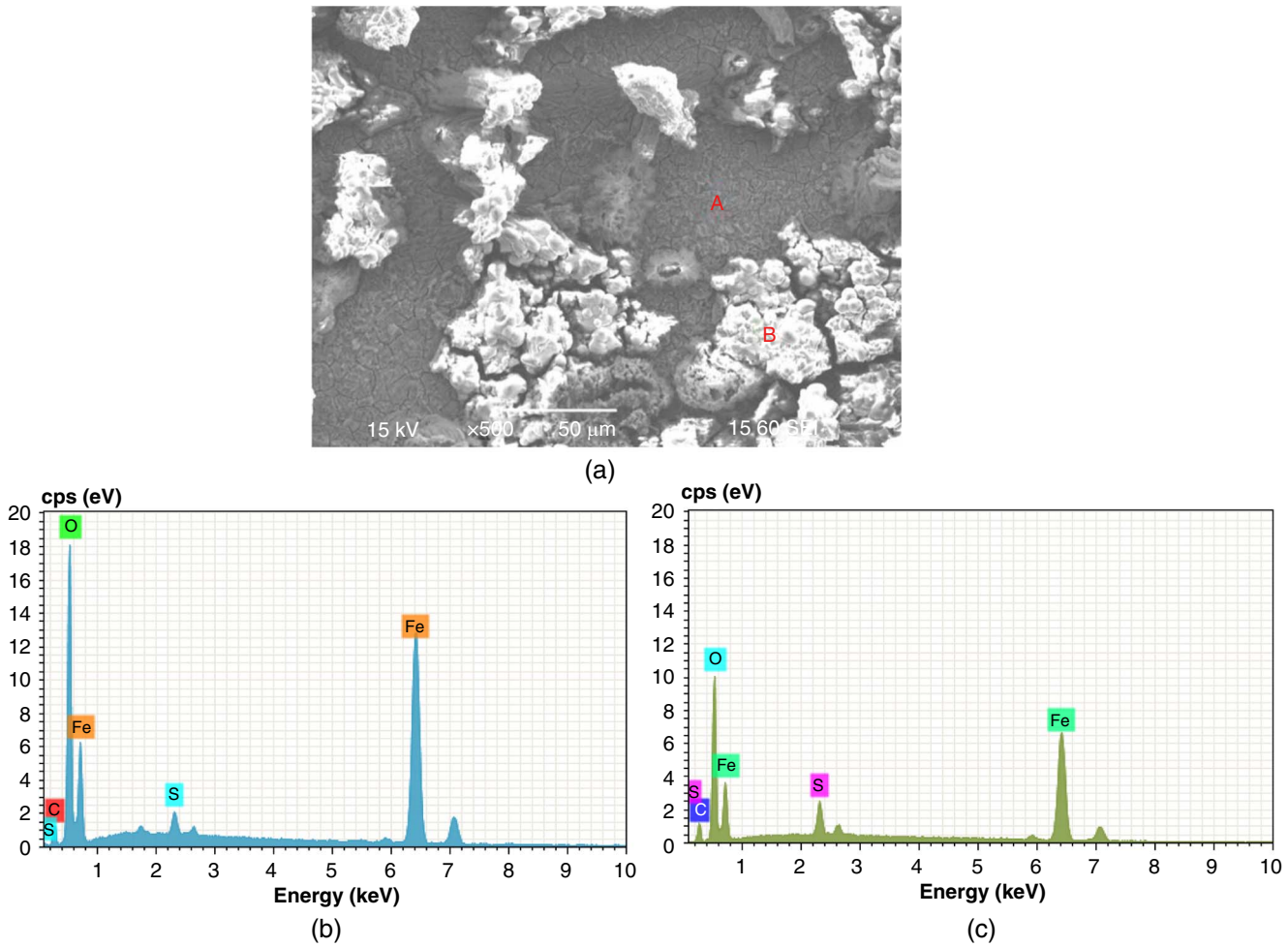

FIGURE 5. *SEM image and EDS spectra of the corroded surface of a sample exposed to the supercritical CO_2 phase with 650 ppm_v H_2O, 4,500 ppm_v SO_2, 100 ppm_v NO, and 40,000 ppm_v O_2 for 48 h (test 4): (a) SEM surface image, (b) EDS spectrum of location A, and (c) EDS spectrum of location B.*

FIGURE 6. *Picture of the surface of the samples after cleaning: (a) test 2: 4,500 ppm$_v$ SO_2, (b) test 3: 50 ppm$_v$ SO_2 + 40,000 ppm$_v$ O_2, and (c) test 4: 4,500 ppm$_v$ SO_2 + 40,000 ppm$_v$ O_2.*

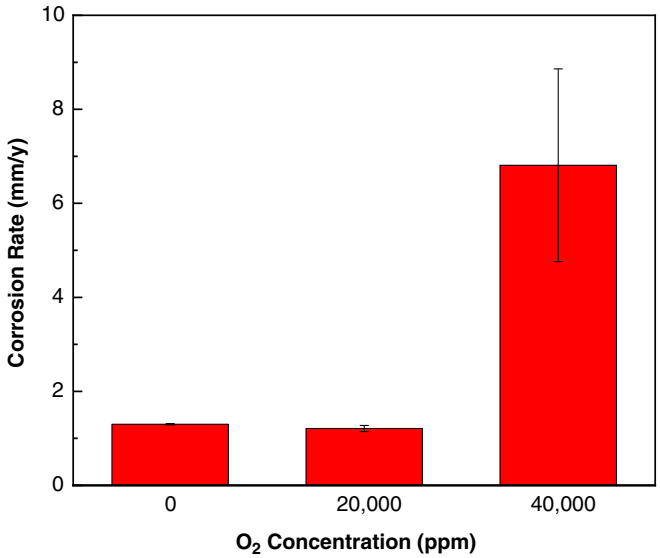

FIGURE 7. *Corrosion rates of carbon steel under flowing supercritical CO_2 with different O_2 concentrations (650 ppm$_v$ H_2O, 4,500 ppm$_v$ SO_2, and 100 ppm$_v$ NO).*

Figure 8 shows the SEM image and EDS spectra of the surface of the sample from test 5 after 48 h exposure in the flowing supercritical CO_2 phase with 650 ppm$_v$ H_2O, 4,500 ppm$_v$ SO_2, and 100 ppm$_v$ NO. The surface was covered with a dense and globular crystalline corrosion product. EDS analyses of corrosion products showed that they comprised mainly of Fe (23.24 at%), S (26.38 at%), and O (39.70 at%), indicating a likely formation of $FeSO_3$. Compared with the surface morphology in the absence of flow (Figure 3), it is obvious that corrosion was accelerated due to the presence of flow, and thus more corrosion products were formed on the steel surface. Figure 9 represents the results of high-resolution optical profilometry analysis on the "cleaned," corrosion product free, sample. Although the presence of flow increased the general corrosion rate, no localized corrosion was observed on the surface (uniform corrosion) in the absence of O_2.

Figure 10 shows the SEM image and EDS spectra of the surface of the sample from test 6 after 48 h of exposure in the flowing supercritical CO_2 phase with 650 ppm$_v$ H_2O, 4,500 ppm$_v$ SO_2, 100 ppm$_v$ NO, and 20,000 ppm$_v$ O_2. The surface was covered with nonuniform corrosion products. EDS analyses of corrosion products showed that both inner layer (location A) and outer island (location B) corrosion products mainly consisted of Fe, C, S, and O, but the outer corrosion product has more S (Table 5). Iron carbonate ($FeCO_3$) has not been found

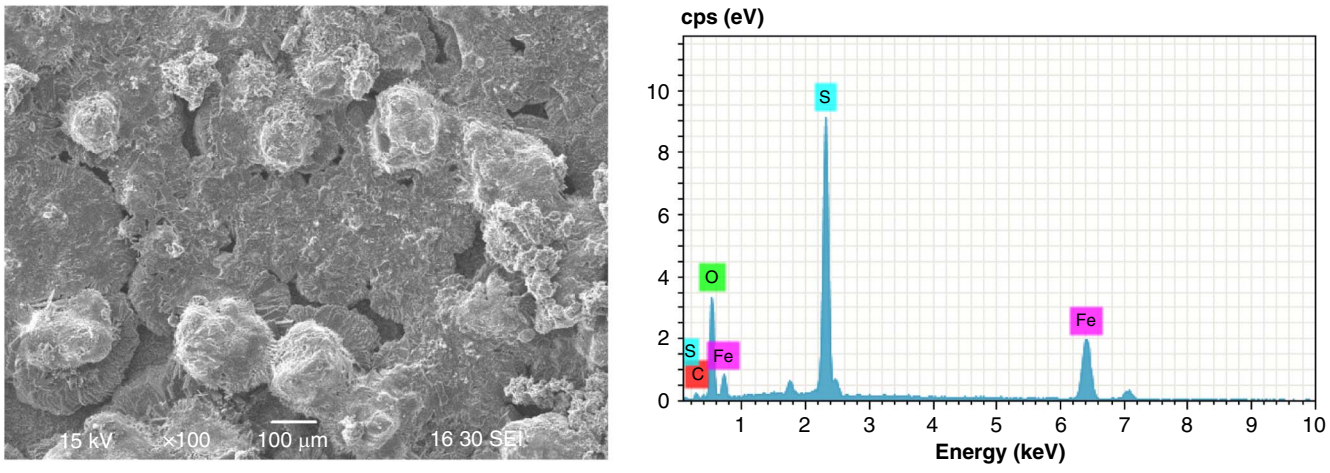

FIGURE 8. *(a) SEM image and (b) EDS spectrum of the corroded surface of a sample exposed to the flowing supercritical CO_2 phase with 650 ppm$_v$ H_2O, 4,500 ppm$_v$ SO_2, and 100 ppm$_v$ NO for 48 h (test 5).*

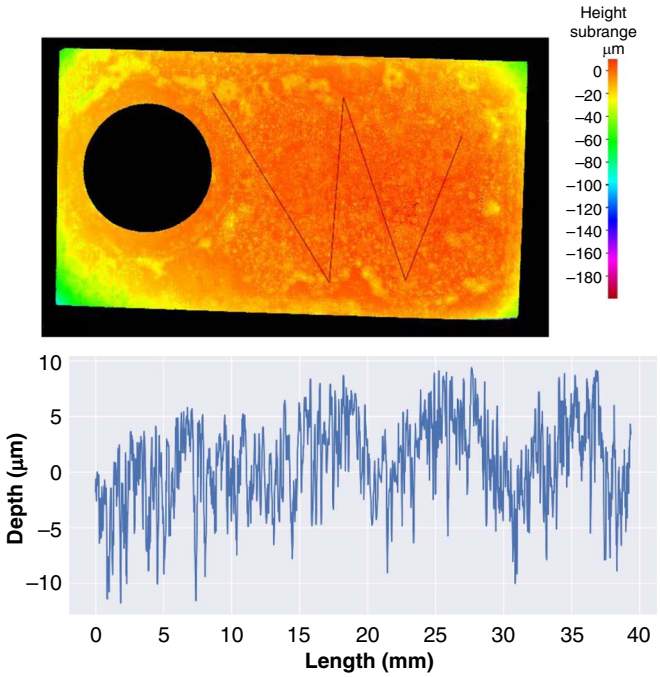

FIGURE 9. *Optical profilometry analysis of the sample surface exposed to the flowing supercritical CO_2 phase with 650 ppm_v H_2O, 4,500 ppm_v SO_2, and 100 ppm_v NO for 48 h.*

under similar conditions; thus, the origin of C is presumed to be a carbide like Fe_3C, not $FeCO_3$. Similar to the results of test 4, the S content was detected as being very low compared to O. It is believed that the formation of oxides occurred even in the presence of flow. Figure 11 presents the results of high-resolution optical profilometry analysis of several pits observed on the cleaned sample. Pits that were not seen in previous results were observed on the specimen surface. According to the depth of the deepest pit (92.8 µm), the maximum localized corrosion rate was calculated to be 16.9 mm/y, which is almost 13 times higher than the general corrosion rate, indicating that the presence of O_2 and flow caused localized corrosion under this condition.

Figure 12 shows the SEM image and EDS spectra of the surface of the sample from test 7 after 48 h exposure in the flowing supercritical CO_2 phase with 650 ppm_v H_2O, 4,500 ppm_v SO_2, 100 ppm_v NO, and 40,000 ppm_v O_2. Similar to the condition with 20,000 ppm_v O_2, the surface was covered with nonuniform corrosion products. EDS analyses of corrosion products showed that inner (location A) corrosion products mainly consisted of Fe, C, S, and O, whereas the outer (location B) corrosion products mainly consisted of Fe, C, and O. In order to confirm the formation of oxides, further phase characterization on the surface of the sample was performed. The result from Raman microscopy analysis of the corroded surface is presented in Figure 13. The spectrum in this figure gives information about the top layer of the corrosion product and shows that it consists of α-FeOOH.[25-26] The absence of peaks between 800 cm^{-1} and 1,300 cm^{-1} means there no carbonate, sulfite, or sulfate-containing corrosion products are present, with the caveat that Raman is highly surface specific. Figure 14 presents the results of high-resolution optical profilometry analysis of several pits observed on the cleaned samples from test 7 exposed to the flowing supercritical CO_2 phase with 650 ppm_v H_2O, 4,500 ppm_v SO_2, 100 ppm_v NO, and 40,000 ppm_v O_2 for 48 h. According to the depth of the deepest pit (170.5 µm), the maximum localized corrosion rate was calculated to be 31.1 mm/y, which is almost four times higher than the general corrosion rate, indicating again that the presence of O_2 and flow caused localized corrosion.

To investigate the effect of SO_2 concentration on the corrosion behavior in the presence of O_2 and flow, an additional test was conducted with 50 ppm_v of SO_2 (test 8). Figure 15 shows the SEM image and EDS spectra of the surface of the sample from test 8 after 48 h of exposure. The surface was covered with a dense inner corrosion product and a loose outer corrosion product. EDS analyses of corrosion products showed that both inner and outer corrosion products mainly consisted of Fe, S, and O, but the outer corrosion product has more S and O (Table 6). Figure 16 presents the result of high-resolution optical profilometry analysis of several pits observed on the cleaned samples from test 8 exposed to the flowing supercritical CO_2 phase with 650 ppm_v H_2O, 50 ppm_v SO_2, 100 ppm_v NO, and 40,000 ppm_v O_2 for 48 h. Even when the concentration of SO_2 was low, localized corrosion was observed in the presence of O_2 and flow. According to the depth of the deepest pit (39.8 µm), the maximum localized corrosion rate was measured to be 7.3 mm/y which is about eight times higher than the uniform corrosion rate (0.95 mm/y).

DISCUSSION

It is important to minimize any possible artifacts that may occur during the corrosion test in the supercritical CO_2 phase with impurities. In the present study, high-purity CO_2 which contains less than 3 ppm of H_2O was used as a CO_2 source to prevent additional H_2O ingress. After each experiment, the autoclave was cleaned and completely dried by using a desiccant. All experiments followed the same pressurizing and depressurizing procedures including impurity injection. Furthermore, gas samples taken from the autoclave for the measurement of SO_2 and NO_2 concentrations were passed through the heated stainless steel lines in order to minimize water/acid condensation.

Table 7 shows the summary of the autoclave corrosion tests conducted in the present study. In the supercritical CO_2 phase (8 MPa, 35°C) with 650 ppm_v H_2O and 100 ppm_v NO, the corrosion rates and corrosion types depended on the SO_2 and O_2 concentrations, and the presence of flow. Table 8 shows the concentrations of SO_2 and NO_2 measured by using colorimetric tubes at the end of the tests. The concentrations shown at the beginning of the tests are the target concentrations of SO_2 and NO for each condition.

No corrosion was observed in the stagnant supercritical CO_2 phase with 50 ppm_v SO_2 and 100 ppm_v NO (test 1), despite a small decrease in SO_2 concentration during the testing period as shown in Table 8. The corrosion rates increased from 0 mm/y to 0.16 mm/y with increasing SO_2 content from 50 ppm_v to 4,500 ppm_v in the stagnant condition (test 2). This indicates that the increase of SO_2 concentration results in the formation of sulfurous acid (H_2SO_3) which affected the corrosion of carbon steel at a water-unsaturated condition in the supercritical CO_2 phase:[24]

$$SO_2 + H_2O \leftrightarrow H_2SO_3 \quad (4)$$

The formation of corrosion product containing Fe, S, and O (Figure 4) also indicates that H_2SO_3 was involved in the corrosion reaction via the following reaction:

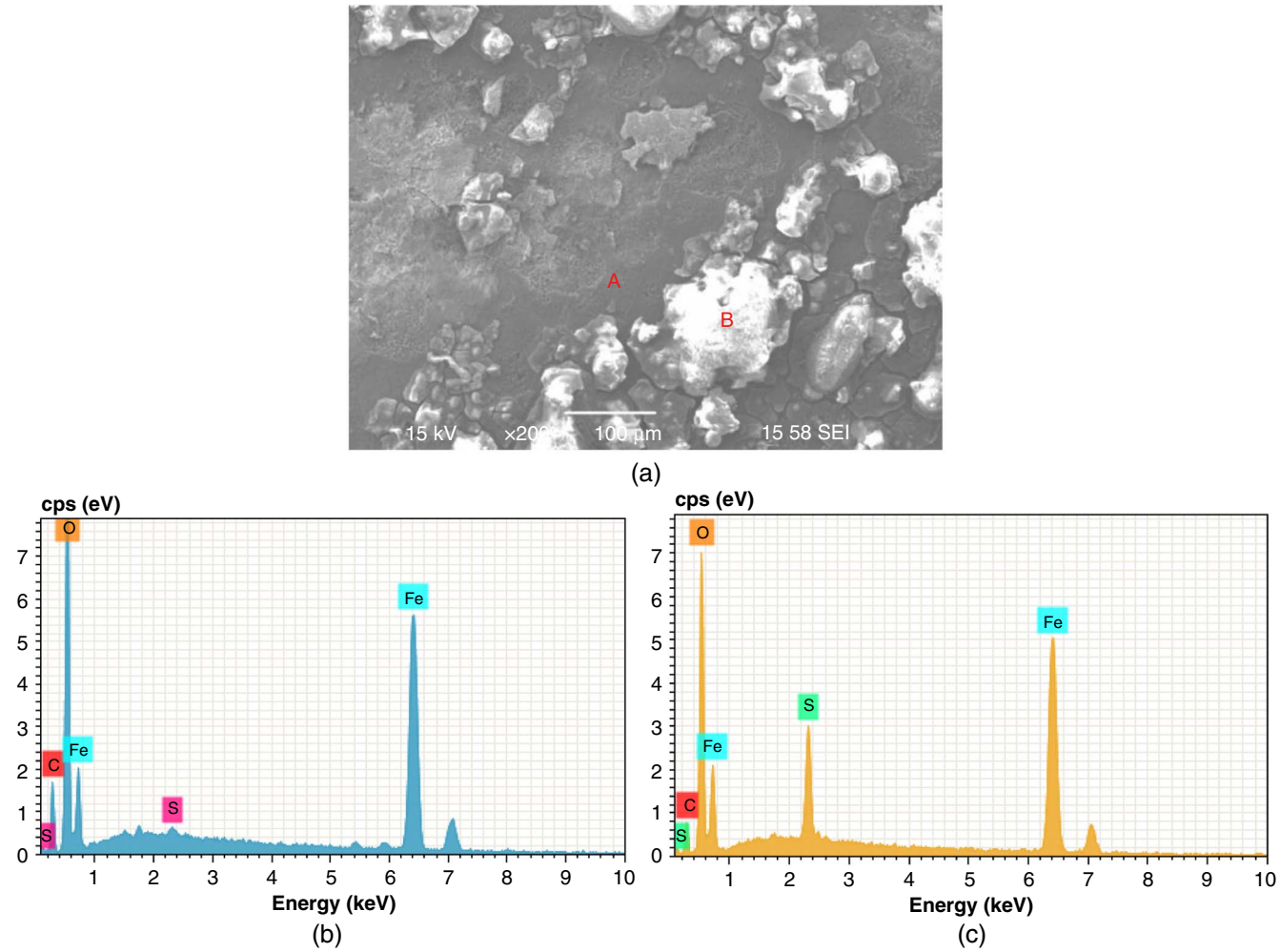

FIGURE 10. *SEM image and EDS spectra of the corroded surface of a sample exposed to the flowing supercritical CO_2 phase with 650 ppm_v H_2O, 4,500 ppm_v SO_2, 100 ppm_v NO, and 20,000 ppm_v O_2 for 48 h (test 6): (a) SEM surface image, (b) EDS spectrum of location A, and (c) EDS spectrum of location B.*

Table 5. *EDS Quantitative Analysis for Different Locations of the Corroded Surface Shown in Figure 10 (Test 6)*

At%	Fe	C	S	O
A	38.36	20.49	0.28	40.87
B	41.45	13.16	5.02	40.37

$$Fe^{2+} + SO_3^{2-} \leftrightarrow FeSO_3 \quad (5)$$

With low SO_2 content (50 ppm_v), the addition of 40,000 ppm_v O_2 slightly affected the corrosion rate (test 3), however, the corrosion rate increased from 0.16 mm/y to 0.42 mm/y in the presence of 4,500 ppm_v SO_2 and 40,000 ppm_v O_2 under stagnant condition (test 4). When O_2 is present in the environment with SO_2, H_2SO_3 further oxidizes to sulfuric acid (H_2SO_4). Furthermore, as shown in Table 8, NO_2 was generated in both test 3 and test 4 indicating that NO reacted with O_2 according to Reaction (6):[27]

$$2NO + O_2 \leftrightarrow 2NO_2 \quad (6)$$

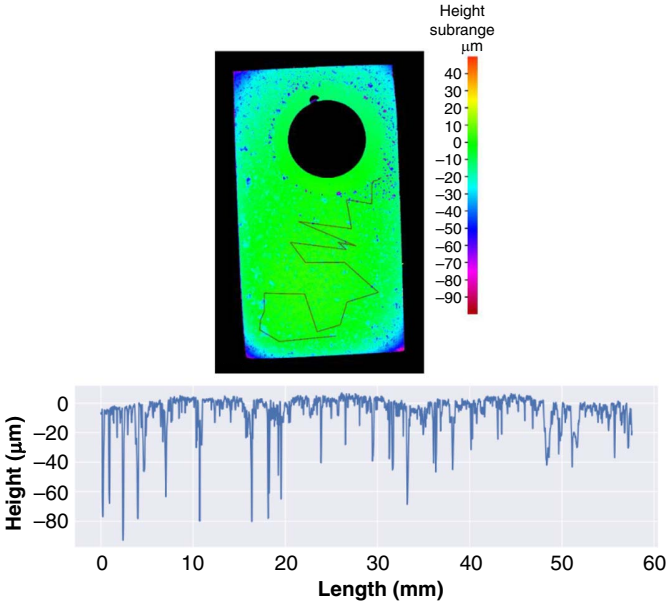

FIGURE 11. *Optical profilometry analysis of the sample surface exposed to the flowing supercritical CO_2 phase with 650 ppm_v H_2O, 4,500 ppm_v SO_2, 100 ppm_v NO, and 20,000 ppm_v O_2 (test 6) for 48 h.*

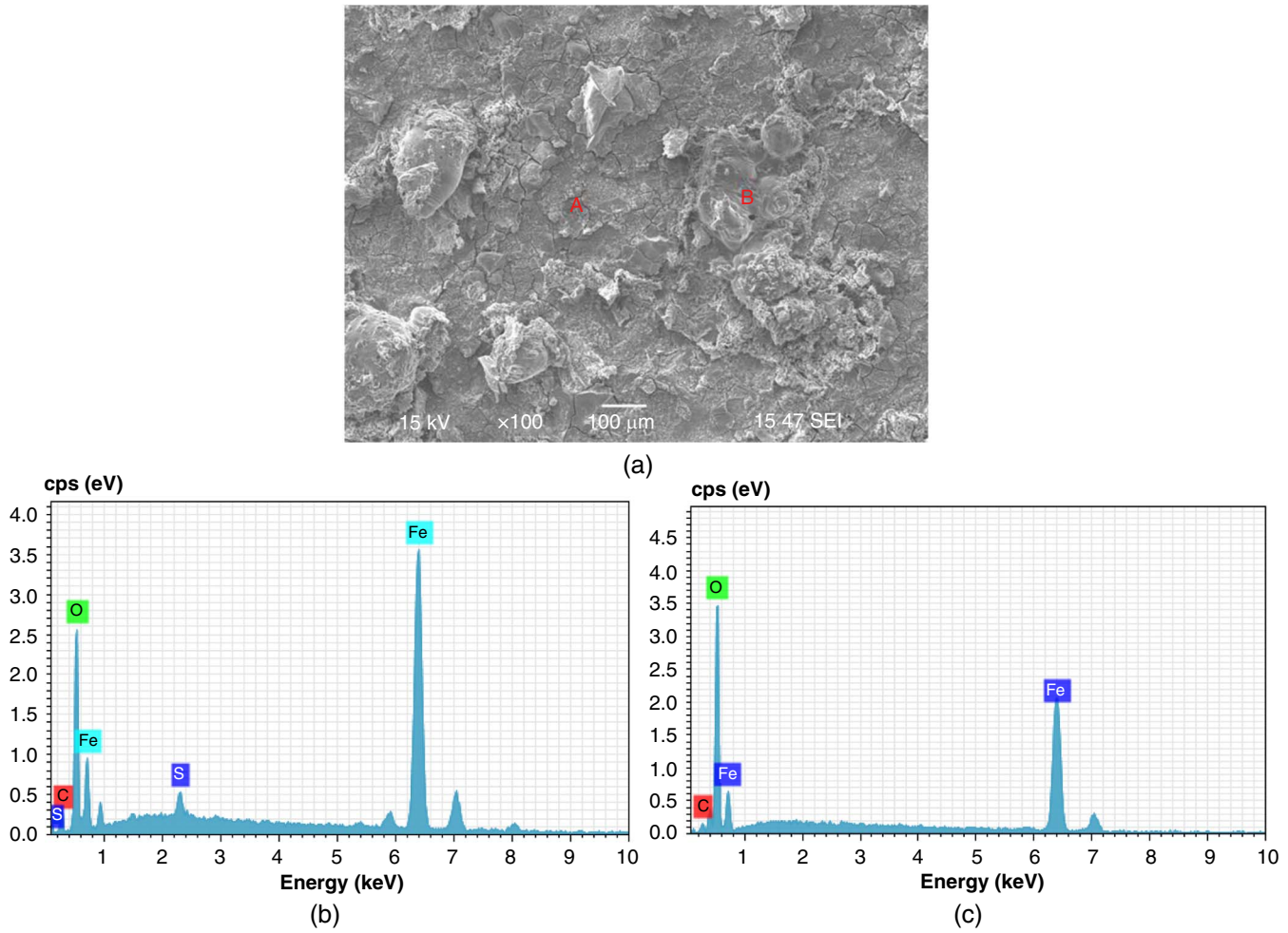

FIGURE 12. *SEM image and EDS spectra of the corroded surface of a sample exposed to the flowing supercritical CO_2 phase with 650 ppm_v H_2O, 4,500 ppm_v SO_2, 100 ppm_v NO, and 40,000 ppm_v O_2 for 48 h (test 7): (a) SEM surface image, (b) EDS spectrum of location A, and (c) EDS spectrum of location B.*

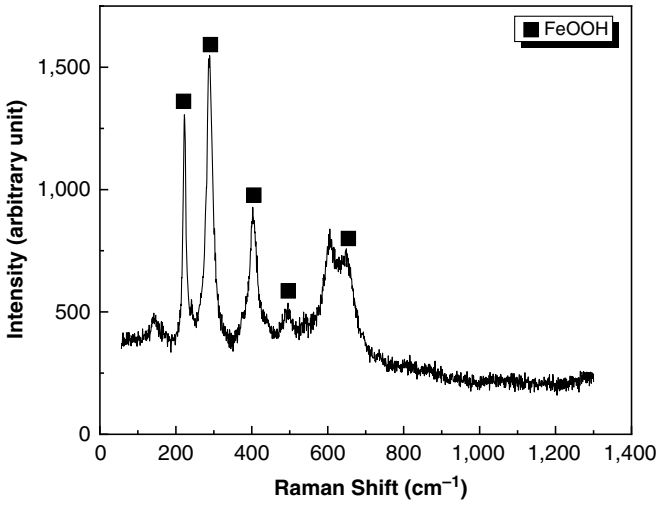

FIGURE 13. *Raman spectrum of the corroded surface of a sample exposed to the flowing supercritical CO_2 phase with 650 ppm_v H_2O, 4,500 ppm_v SO_2, 100 ppm_v NO, and 40,000 ppm_v O_2 for 48 h (test 7).*

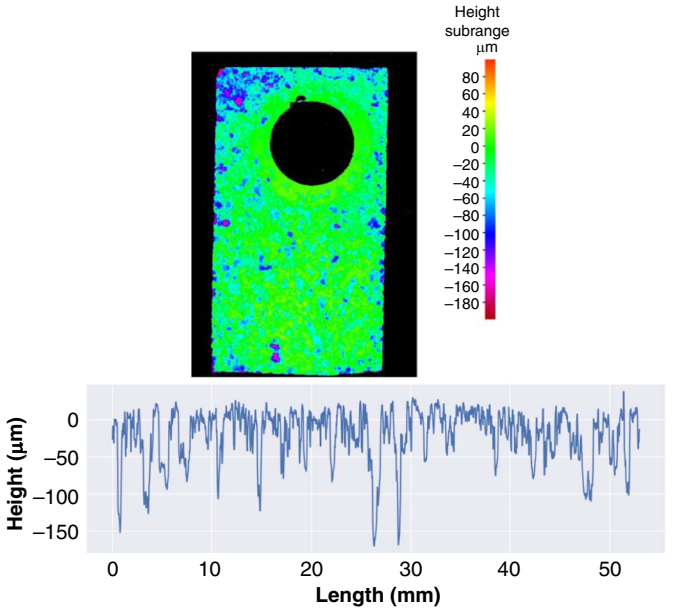

FIGURE 14. *Optical profilometry analysis of the sample surface exposed to the flowing supercritical CO_2 phase with 650 ppmv H_2O, 4,500 ppmv SO_2, 100 ppmv NO, and 40,000 ppmv O_2 for 48 h.*

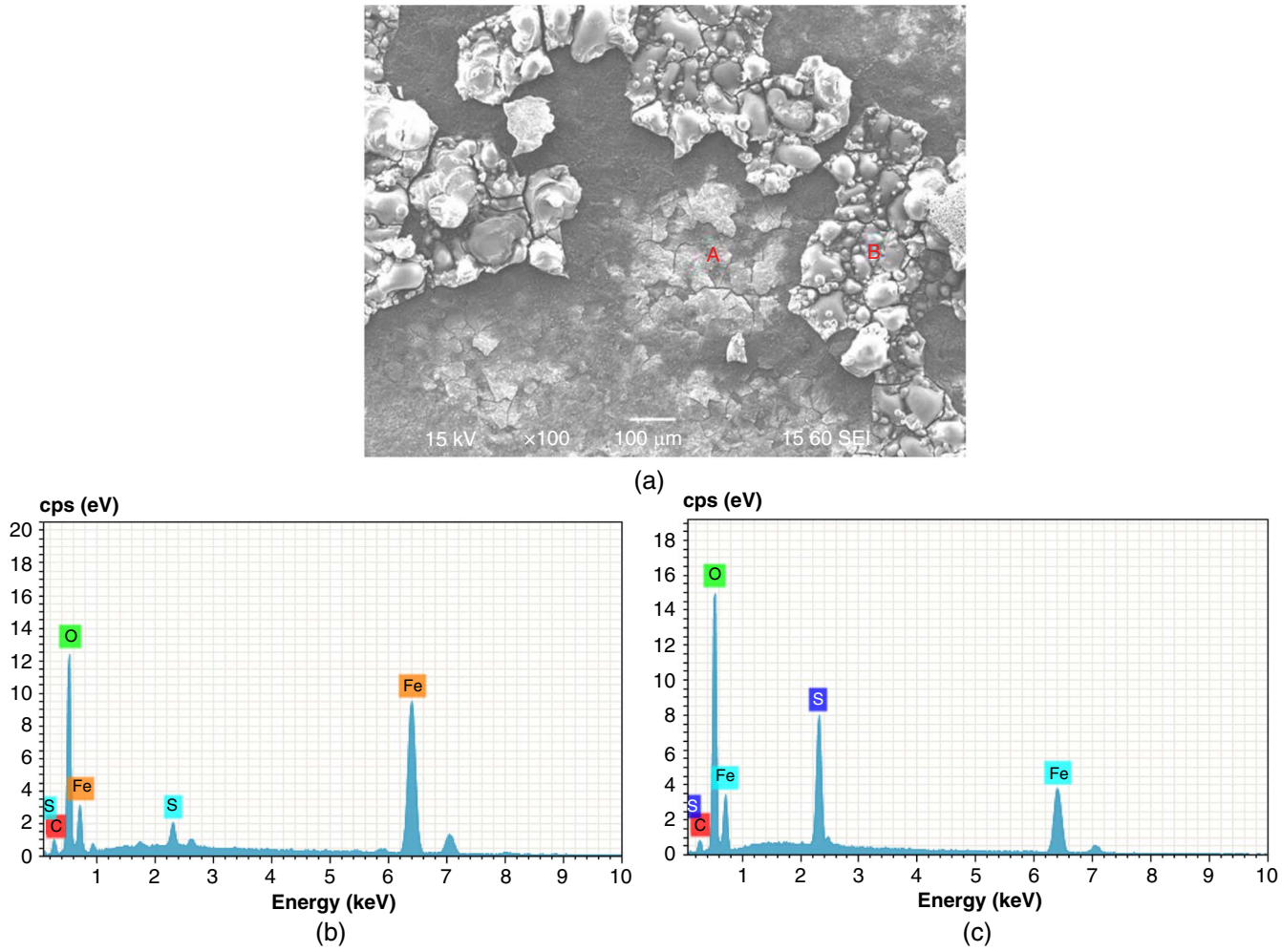

FIGURE 15. *SEM image and EDS spectra of the corroded surface of a sample exposed to the flowing supercritical CO_2 phase with 650 ppm_v H_2O, 50 ppm_v SO_2, 100 ppm_v NO, and 40,000 ppm_v O_2 for 48 h (test 8): (a) SEM surface image, (b) EDS spectrum of location A, and (c) EDS spectrum of location B.*

Table 6. *EDS Quantitative Analysis for Different Locations of the Corroded Surface Shown in Figure 15 (Test 8)*

At.%	Fe	C	S	O
A	46.89	9.76	1.97	41.39
B	19.97	10.34	9.10	60.59

Morland, et al., postulated a reaction for H_2SO_4 formation in the presence of NO_2:[27]

$$SO_2 + H_2O + NO_2 \leftrightarrow H_2SO_4 + NO \quad (7)$$

They also stated that the oxidation of H_2SO_3 to H_2SO_4 by O_2 is much slower than the Reaction (7). Thus, it can be considered that Reactions (6) and (7) were the main chemical reactions in test 3 and test 4. As NO is regenerated when H_2SO_4 is formed, it can be seen that high O_2 concentration might give an eternal cycle of the formation of NO_2 until all of the SO_2 or H_2O are consumed by chemical and corrosion reactions. H_2SO_4 reacts with Fe according to the following reaction:

$$Fe + H_2SO_4 \leftrightarrow FeSO_4 + H_2 \quad (8)$$

As the specific analysis of corrosion products was not performed in the present study, the exact compositions of the corrosion products shown in Figures 4 and 5 are not known. However, it can be assumed that $FeSO_4$ was formed through the results of EDS analysis. In addition, the high oxygen concentration in the corrosion product through EDS analysis (Table 4) indicates that $FeSO_4$ could be oxidized to FeOOH according to the Reaction (9),[28-29] and the H_2SO_4 produced by the acid regeneration cycle continues to react with the fresh steel, resulting in the high corrosion rate in the presence of both SO_2 and O_2 as claimed in our previous study.[24]

$$4FeSO_4 + 6H_2O + O_2 \leftrightarrow 4FeOOH + 4H_2SO_4 \quad (9)$$

The presence of flow significantly accelerated the corrosion of carbon steel. The corrosion rate increased from 0.16 mm/y to 1.30 mm/y with 4,500 ppm_v SO_2, and NO_2 was not generated since no O_2 was added (test 5). No significant difference in the corrosion rate was observed with 20,000 ppm_v of O_2 in the flowing supercritical CO_2 (test 6), however, it significantly increased to 6.81 mm/y with

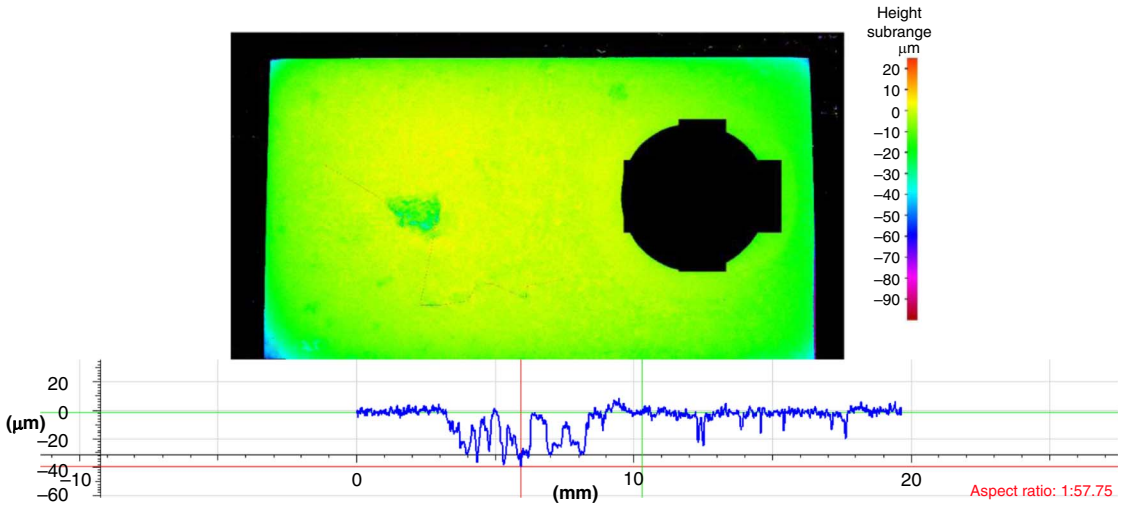

FIGURE 16. *Optical profilometry analysis of the sample surface exposed to the flowing supercritical CO_2 phase with 650 ppm_v H_2O, 50 ppm_v SO_2, 100 ppm_v NO, and 40,000 ppm_v O_2 (test 8) for 48 h.*

Table 7. *Summary of the Autoclave Corrosion Tests*

Test	pCO_2 (MPa)	Temperature (°C)	H_2O (ppm_v)	SO_2 (ppm_v)	NO (ppm_v)	O_2 (ppm_v)	Flow	Corrosion Rate (mm/y)	Localized Corrosion
1	8	35	650	50	100	0	No	0	No
2	8	35	650	4,500	100	0	No	0.16	No
3	8	35	650	50	100	40,000	No	0.15	No
4	8	35	650	4,500	100	40,000	No	0.42	No
5	8	35	650	4,500	100	0	Yes	1.30	No
6	8	35	650	4,500	100	20,000	Yes	1.21	Yes (16.9 mm/y)
7	8	35	650	4,500	100	40,000	Yes	6.81	Yes (31.1 mm/y)
8	8	35	650	50	100	40,000	Yes	0.95	Yes (7.3 mm/y)

Table 8. *Concentrations of Impurities at the Beginning and End of the Test*

Test	Concentration at the Beginning (ppm_v)		Concentration at the End (ppm_v)	
	SO_2	NO	SO_2	NO_2
1	50	100	20	0
2	4,500	100	–	–
3	50	100	5	4
4	4,500	100	>100	20
5	4,500	100	500	0
6	4,500	100	0	10
7	4,500	100	50	10
8	50	100	0	80

40,000 ppm_v O_2 (test 7). Such an acceleration of corrosion in the presence of flow can also be clearly identified from the SEM images of the samples. Compared with the surface morphology at the stagnant condition, it seems that the surface covered by the corrosion product layers becomes larger at the flowing condition, as can be seen from Figures 5 and 12. Furthermore, it is noteworthy that almost all SO_2 was consumed in the presence of both O_2 and flow (Table 8), indicating the promotion of H_2SO_4 formation (Reaction [7]). However, considering the impurity concentrations in the test condition, the concentration of H_2O should dominate the Reaction (7) since the H_2O content (650 ppm_v) is much lower than the SO_2 content (4,500 ppm_v). This implies that 4,500 ppm_v of SO_2 cannot be consumed by the Reaction (7) unless there is another reaction that can generate H_2O.

It has been recently shown by experimental and modeling that H_2SO_4 dropout (acid condensation) could occur under water-unsaturated conditions due to the lower solubility of H_2SO_4 compared to H_2O in the dense phase CO_2.[30] These results can also be applied to the present study. Thus, it is postulated that a primary cause of accelerated corrosion due to flow is that the flow increased the chance of condensed acids reaching the surface of the steel specimens. The flowing supercritical CO_2 may aid condensed acid droplets reaching the steel surface, thereby replenishing the acid species required for

corrosion. This mechanism was likewise attributed to accelerated corrosion by Liu, et al.[18]

It is important to note that severe localized corrosion was observed in the presence of both O_2 and flow. A maximum penetration rate of 13.1 mm/y was measured for the condition with 4,500 ppm_v SO_2 and 20,000 ppm_v O_2 (test 6), it further increased to 31.1 mm/y for the condition with 4,500 ppm_v SO_2 and 40,000 ppm_v O_2 (test 7). Localized corrosion was also observed with lower SO_2 concentration (50 ppm_v) with a maximum penetration rate of 7.3 mm/y (test 8). It seems to have resulted from the nonuniform replenishment of acid droplets in the presence of flow, yet the mechanism of localized corrosion is far less certain. Further work is required to examine the relationship of the impurities and flow with localized corrosion as well as the effect of flow on the chemical reactions in the dense-phase CO_2.

CONCLUSIONS

The following conclusions can be drawn from the experimental results conducted in the present study:

➢ Corrosion occurs at water-unsaturated conditions (650 ppm_v H_2O) in supercritical CO_2 (8 MPa and 35°C) with the presence of impurities (SO_2, NO, and O_2).
➢ The corrosion rates depended on the SO_2 and O_2 concentrations, and the presence of flow.
➢ Severe localized corrosion was observed in the presence of both O_2 and flow.

ACKNOWLEDGMENTS

The authors would like to acknowledge the financial support from Ohio Coal Development Office (OCDO) for the Institute for Corrosion and Multiphase Technology at Ohio University.

References

1. V.E. Onyebuchi, A. Kolios, D.P. Hanak, C. Biliyok, V. Manovic, *Renew. Sustain. Energy Rev.* 81 (2018): p. 2563-2583.
2. Global CCS Institute, "The Global Status of CCS" (2013), https://www.globalccsinstitute.com/publications/global-status-ccs-2013.
3. Y. Xiang, Z. Wang, X.X. Yang, Z. Li, W.D. Ni, *J. Supercrit. Fluid* 67 (2012): p. 14-21.
4. Y. Hua, R. Barker, A. Neville, *Int. J. Greenhouse Gas Control* 31 (2014): p. 48-60.
5. Y. Hua, R. Barker, A. Neville, *J. Supercrit. Fluid* 97 (2015): p. 224-237.
6. B.H. Morland, A. Dugstad, G. Svenningsen, *Energy Proc.* 114 (2017): p. 6752-6765.
7. X. Jiang, D. Qu, X. Song, X. Liu, Y. Zhang, *Int. J. Greenhouse Gas Control* 85 (2019): p. 11-22.
8. Y. Hua, R. Barker, A. Neville, *Appl. Surf. Sci.* 356 (2015): p. 499-511.
9. Y. Hua, R. Barker, A. Neville, *Int. J. Greenhouse Gas Control* 37 (2015): p. 412-423.
10. M. Xu, W. Li, Y. Zhou, X.X. Yang, Z. Wang, Z. Li, *Int. J. Greenhouse Gas Control* 51 (2016): p. 357-368.
11. A. Dugstad, M. Halseid, B. Morland, *Energy Proc.* 37 (2013): p. 2877-2887.
12. F. Farelas, Y.S. Choi, S. Nešić, *Corrosion* 69 (2013): p. 243-250.
13. Y.S. Choi, S. Hassani, T.N. Vu, S. Nešić, A.Z.B. Abas, *Corrosion* 72 (2016): p. 999-1009.
14. C. Sun, J. Sun, S. Liu, Y. Wang, *Corros. Sci.* 137 (2018): p. 151-162.
15. B.H. Morland, M. Tjelta, A. Dugstad, G. Svenningsen, *Corrosion* 75 (2019): p. 1307-1314.
16. B.H. Morland, T. Norby, M. Tjelta, G. Svenningsen, *Corrosion* 75 (2019): p. 1327-1338.
17. B.H. Morland, A. Dugstad, G. Svennigsen, *Int. J. Greenhouse Gas Control* 119 (2022): p. 103697.
18. A.Q. Liu, C. Bian, Z.M. Wang, X. Han, J. Zhang, *Corros. Sci.* 134 (2018): p. 149-161.
19. J. S. de Sa, W. Ma, J. Owen, Y. Hua, A. Neville, J.A.C.P. Gomes, R. Barker, *Corrosion* 78 (2022): p. 58-67.
20. D.Y. Peng, D.B. Robinson, *Ind. Eng. Chem. Fundamentals* 15 (1976): p. 59-64.
21. ASTM Standard G31, "Standard Practice for Laboratory Immersion Corrosion Testing of Metals" (West Conshohocken, PA: ASTM International, 1994).
22. DOE/NETL Quality Guidelines for Energy System Studies, "CO_2 Impurity Design Parameters," DOE/NETL-341/011212, 2013.
23. A. Armpriester, "W.A. Parish Post Combustion CO_2 Capture and Sequestration Project Final Public Design Report," United States, 2017, https://www.osti.gov/servlets/purl/1344080.
24. Y.S. Choi, S. Nešić, D. Young, *Environ. Sci. Technol.* 44 (2010): p. 9233-9238.
25. S.J. Oh, D.C. Cook, H.E. Townsend, *Hyperfine Interact.* 112 (1998): p. 59-66.
26. S. Li, L.H. Hihara, *J. Electrochem. Soc.* 162 (2015): p. C495-C502.
27. B.H. Morland, M. Tjelta, T. Norby, G. Svenningsen, *Int. J. Greenhouse Gas Control* 87 (2019): p. 246-255.
28. B.L. Tiwari, J. Kolbe, H.W. Hayden, *Metall. Trans. B* 10 (1979): p. 607-612.
29. R. Nishimura, D. Shiraishi, Y. Maeda, *Corros. Sci.* 46 (2004): p. 225-243.
30. B.H. Morland, A. Tadesse, G. Svenningsen, R.D. Springer, A. Anderko, *Ind. Eng. Chem. Res.* 58 (2019): p. 22924-22933.